

Effect of capillarity and relative permeability on Q anisotropy of hydrocarbon source rocks

J.E. Santos,^{1,2,3} G.B. Savioli,² José M. Carcione⁴ and Jing Ba¹

¹*School of Earth Sciences and Engineering, Hohai University, Nanjing 211100, China. Corresponding Author: Jing Ba. E-mail: jba@hhu.edu.cn*

²*Universidad de Buenos Aires, Facultad de Ingeniería, Instituto del Gas y del Petróleo, Av. Las Heras 2214, Piso 3, Buenos Aires, Argentina*

³*Department of Mathematics, Purdue University, 150 N. University Street, West Lafayette, IN 47907-2067, USA*

⁴*Istituto Nazionale di Oceanografia e di Geofisica Sperimentale (OGS), Borgo Grotta Gigante 42c, 34010 Sgonico, Trieste, Italy*

Accepted 2019 May 10. Received 2019 May 9; in original form 2019 February 20

SUMMARY

Shale reservoir formations are porous rocks of low permeability composed of fluid-saturated illite–smectite and kerogen layers, which behave as viscoelastic transversely isotropic (VTI) media at long wavelengths, that is, much larger than the average layer thickness. Seismic waves travelling across these heterogeneous materials induce wave-induced fluid flow (WIFF) and Biot slow waves generating energy loss (mesoscopic loss) and velocity dispersion. When these formations are saturated by two-phase fluids, the presence of capillary forces—interfacial tension—and interaction between the two fluids as they move within the pore space need to be taken into account. This can be achieved using a Biot model of a poroelastic solid saturated by a two-phase fluid that includes capillary pressure and relative permeability functions and supports the existence of two slow waves. An upscaling finite-element method is used to analyse the WIFF, which determines an effective VTI medium predicting higher attenuation and (Q) anisotropy than the classical single-phase (single fluid) models.

Key words: Numerical approximations and analysis; Numerical modelling; Numerical solutions; Computational seismology; Seismic anisotropy; Seismic attenuation.

1 INTRODUCTION

The purpose of this work is to analyse the anisotropy in seismic attenuation of shale reservoir rocks as a function of fluid saturation and spatial distribution of organic matter (oil and kerogen) in the rock matrix. Most shale reservoir rocks are laminated media (with typical thickness of mm) of very low permeability composed of illite–smectite layers and organic matter in the form of oil, gas and kerogen. For seismic wavelengths much larger than the thickness of the layers, these laminated materials behave as homogeneous viscoelastic transversely isotropic (VTI) media.

Biot (1956a,b; 1962) developed a theory to describe wave propagation in a poroelastic solid saturated by a single-phase fluid (a single-phase Biot medium—SPBM). The theory predicts the existence of two compressional waves (one of them slow), and one shear wave. The fast P wave has solid and fluid motions in phase, and the slow Biot P wave has out-of-phase motion, causing strong energy losses. The existence of the second slow wave was confirmed by Plona (1980). Most recently, Bouzidi & Schmitt (2009) presented experiments where the slow P_2 wave was observed at a wide range of incident angles.

However, Biot's theory does not take into account the presence of capillary forces and interference effects between the two flu-

ids as they move within the pore space. A generalization of Biot's theory to the case when a poroelastic medium is saturated by a two-phase fluid (a two-phase Biot medium—2PBM) was presented in Santos *et al.* (1990a,b) and Ravazzoli *et al.* (2003). The 2PBM model includes effects of capillary and relative permeability functions defined in terms of the two-phase Darcy's law (Scheidegger 1974; Peaceman 1977). The model predicts the existence of one fast wave, two slow compressional waves and one shear wave. Capillary forces are responsible for the existence of one additional slow wave, while relative permeability functions induce energy losses due to interferences between the two-phase fluids as they move within the pores. The work by Müller & Sahay (2011) presents an extension of Biot's theory for single-phase fluids predicting the existence of a second slow shear wave.

Among others, Dutta & Odé (1979), Mochizuki (1982), Berryman *et al.* (1988) and Toksöz *et al.* (1976) tackled the analysis of the quasi-static and dynamic behaviour of porous rocks with partial, miscible or segregated fluid saturation. None of the above approaches incorporate the capillary forces. Using a homogenization approach, Auriault (1989) included a description of capillary effects at the pore scale obtaining a two-phase Darcy law.

One significant cause of attenuation in layered fluid-saturated poroelastic media is wave-induced fluid flow (WIFF), by which the

fast compressional (P) and shear (S) waves are converted to slow (diffusive) Biot waves as they travel across regions with heterogeneities in the fluid and petrophysical properties of the medium. We refer to this mechanism as mesoscopic loss envisioning the length scale of the heterogeneities to be larger than the grain sizes but much smaller than the wavelength of the pulse. For instance, if the matrix porosity varies significantly from point to point, diffusion of pore fluid between different regions constitutes a mechanism that can be important at seismic frequencies. Pride *et al.* (2004) have demonstrated the importance of the mesoscopic effects in the context of exploration geophysics as being the dominant P -wave attenuation mechanism in reservoir rocks at seismic frequencies.

A review of the different theories and authors, who have contributed to the understanding of this mechanism, can be found, for instance, in Carcione & Picotti (2006), Müller *et al.* (2010) and Carcione (2014). In this work, the analysis of the WIFF takes into account the presence of two slow waves and the additional energy losses present in the case of two-phase fluids.

For an analysis of anisotropy in stratified media, we mention the early work by Carcione *et al.* (1991), whereas Carcione *et al.* (2011) treated the specific case of source rocks without energy loss. Gelinisky & Shapiro (1997) obtained the relaxed and unrelaxed stiffnesses of a poroviscoelastic medium equivalent to a finely layered SPBM. Assuming that the layers are homogeneous and flow is perpendicular to the layering plane, Krzikalla & Müller (2011) obtained the five complex and frequency-dependent stiffnesses of a VTI medium equivalent to a layered SPBM.

Qi *et al.* (2014) studied the effects of capillarity on attenuation and dispersion in isotropic patchy-saturated rocks and found that the capillary action leads to an additional stiffening and thereby to higher phase velocities, with weakening diffusion process and attenuation.

The work in Santos & Carcione (2015) uses the SPBM model to define a set of five harmonic compressibility and shear experiments for determining the stiffness coefficients and the corresponding energy velocities and dissipation factors of a long-wave equivalent VTI medium to a densely fractured fluid-saturated poroelastic medium. The numerical experiments are formulated as boundary value problems (BVP) in the space–frequency domain that are solved using the finite-element (FE) method. See also Santos & Gauzellino (2017) for a detailed description of the use of the FE method in the context of numerical rock physics and upscaling.

2 THE MODEL DESCRIBING A POROELASTIC MEDIUM SATURATED BY A TWO-PHASE FLUID

In a porous solid saturated by a two-phase fluid exist *wetting* and *non-wetting* phases denoted with the subscripts (or superscripts) ‘w’ and ‘n’, respectively, while ‘s’ will indicate the solid phase. Let S_l and S_{rl} be the saturation and residual saturation of the l -phase, $l = n, w$, so that $S_{rn} < S_n < 1 - S_{rw}$. Besides, we assume full saturation of the pore space, $S_w + S_n = 1$ (Scheidegger 1974; Peaceman 1977). In the shale reservoir model studied in this work, gas is always the non-wetting phase (see Fig. 1).

The relative particle fluid displacements are

$$\mathbf{u}^l = \phi(\tilde{\mathbf{u}}^l - \mathbf{u}^s), \quad \xi^l = -\nabla \cdot \mathbf{u}^l, \quad l = n, w,$$

where $\mathbf{u}^s = (u_i^s)$, $\tilde{\mathbf{u}}^l = (\tilde{u}_i^l)$, $l = n, w$, $i = 1, 2, 3$ are the time Fourier transforms of the displacement vectors of the solid and fluid phases and ϕ is the matrix effective porosity.

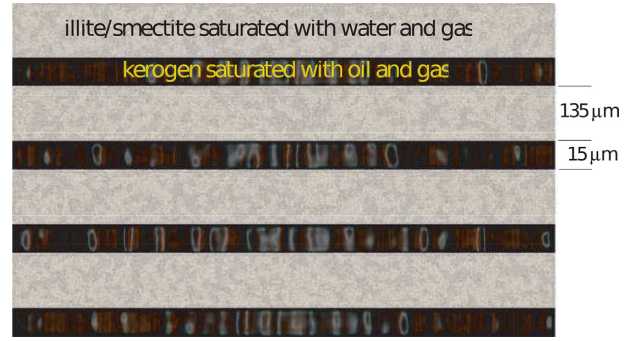


Figure 1. Schematic model of the Vaca Muerta formation.

Define $\varepsilon_{ij}(\mathbf{u}^s)$ and $e^s = \varepsilon_{ii}(\mathbf{u}^s)$ as the Fourier transforms of the strain tensor of the solid and its linear invariant, respectively, and set $\mathbf{u} = (\mathbf{u}^s, \mathbf{u}^n, \mathbf{u}^w)$. Let $\boldsymbol{\tau} = \tau_{ij}$ and $\boldsymbol{\varepsilon} = \varepsilon_{ij}$, $i, j = 1, 2, 3$ denote the time Fourier transforms of the stress and strain tensors, respectively. Also, let P_l denote the time Fourier transform of the infinitesimal change in the pressure of the l -fluid phase, taken with respect to the reference value $\bar{P}_l |_{l = n, w}$. This reference value is associated with the initial equilibrium state having non-wetting fluid saturation \bar{S}_n and porosity $\bar{\phi}$. P_n and P_w are related through the capillary relation (Scheidegger 1974; Peaceman 1977):

$$\begin{aligned} P_{ca} &= P_{ca}(S_n + \bar{S}_n) = \bar{P}_n + P_n - (\bar{P}_w + P_w) \\ &= P_{ca}(\bar{S}_n) + P_n - P_w \geq 0. \end{aligned} \quad (1)$$

The stress–strain relations of a 2PBM are (Santos *et al.* 1990a; Ravazzoli *et al.* 2003)

$$\tau_{ij}(\mathbf{u}) = 2N \varepsilon_{ij} + \delta_{ij}(\lambda_u e^s - B_1 \xi^n - B_2 \xi^w), \quad (2)$$

$$\begin{aligned} \mathcal{T}_n(\mathbf{u}) &= (\bar{S}_n + \beta + \zeta) P_n - (\beta + \zeta) P_w \\ &= -B_1 e^s + M_1 \xi^n + M_3 \xi^w, \end{aligned} \quad (3)$$

$$\mathcal{T}_w(\mathbf{u}) = (\bar{S}_w + \zeta) P_w - \zeta P_n = -B_2 e^s + M_3 \xi^n + M_2 \xi^w, \quad (4)$$

where

$$\beta = \frac{P_{ca}(\bar{S}_n)}{P'_{ca}(\bar{S}_n)}, \quad \zeta = \frac{\bar{P}_w}{P'_{ca}(\bar{S}_n)}. \quad (5)$$

The coefficient N is the shear modulus of the dry rock. The determination of the other coefficients in eqs (2)–(4) is explained in Santos *et al.* (1990a), Ravazzoli *et al.* (2003) and Santos & Gauzellino (2017).

The governing equations for a 2PBM in the diffusive range of frequencies are

$$\frac{\partial \tau_{ij}}{\partial x_j} = 0, \quad (6)$$

$$i\omega(\bar{S}_n)^2 \frac{\eta_n}{\kappa K_{rn}(\bar{S}_n)} u_j^n - i\omega d_{nw} u_j^w + \frac{\partial \mathcal{T}_n}{\partial x_j} = 0, \quad (7)$$

$$i\omega(\bar{S}_w)^2 \frac{\eta_w}{\kappa K_{rw}(\bar{S}_w)} u_j^w - i\omega d_{nw} u_j^n + \frac{\partial \mathcal{T}_w}{\partial x_j} = 0, \quad j = 1, 2, 3. \quad (8)$$

The cross dissipative coefficient d_{nw} is taken to be

$$d_{nw}(\bar{S}_n, \bar{S}_w) = \left((\bar{S}_n)^2 \frac{\eta_n}{\kappa K_{rn}(\bar{S}_n)} \right) \left((\bar{S}_w)^2 \frac{\eta_w}{\kappa K_{rw}(\bar{S}_w)} \right). \quad (9)$$

In eqs (7) and (8), η_n, η_w are the fluid viscosities and $\kappa, K_m(S_n), K_{rw}(S_w)$ are the absolute and relative permeabilities, respectively. In this work, the following relative permeability and capillary pressure functions are used (Ravazzoli *et al.* 2003):

$$\begin{aligned} K_m(S_n) &= (1 - (1 - S_n)/(1 - S_m))^2, \\ K_{rw}(S_n) &= ([1 - S_n - S_{rw}]/(1 - S_{rw}))^2, \\ P_{ca}(S_n) &= A(1/(S_n + S_{rw} - 1)^2 - S_m^2/[S_n(1 - S_m - S_{rw})]^2), \end{aligned} \quad (10)$$

where A is the capillary pressure amplitude, chosen to be 30 kPa.

3 THE EQUIVALENT VISCOELASTIC TRANSVERSELY ISOTROPIC MEDIUM

As shown in Krzikalla & Müller (2011), a fluid-saturated poroelastic solid with a set of horizontal layers behaves as a VTI medium with vertical symmetry axis at long wavelengths.

Denoted by $\sigma_{ij}(\tilde{\mathbf{u}}_s)$ and $e_{ij}(\tilde{\mathbf{u}}_s)$ the stress and strain tensor components of the equivalent VTI medium, where $\tilde{\mathbf{u}}_s$ denotes the solid displacement vector at the macroscale. The corresponding stress–strain relations, stated in the space–frequency domain and assuming a closed system are (Carcione, 2014)

$$\sigma_{11}(\tilde{\mathbf{u}}_s) = p_{11} e_{11}(\tilde{\mathbf{u}}_s) + p_{12} e_{22}(\tilde{\mathbf{u}}_s) + p_{13} e_{33}(\tilde{\mathbf{u}}_s), \quad (11)$$

$$\sigma_{22}(\tilde{\mathbf{u}}_s) = p_{12} e_{11}(\tilde{\mathbf{u}}_s) + p_{11} e_{22}(\tilde{\mathbf{u}}_s) + p_{13} e_{33}(\tilde{\mathbf{u}}_s), \quad (12)$$

$$\sigma_{33}(\tilde{\mathbf{u}}_s) = p_{13} e_{11}(\tilde{\mathbf{u}}_s) + p_{13} e_{22}(\tilde{\mathbf{u}}_s) + p_{33} e_{33}(\tilde{\mathbf{u}}_s), \quad (13)$$

$$\sigma_{23}(\tilde{\mathbf{u}}_s) = 2 p_{55} e_{23}(\tilde{\mathbf{u}}_s), \quad (14)$$

$$\sigma_{13}(\tilde{\mathbf{u}}_s) = 2 p_{55} e_{13}(\tilde{\mathbf{u}}_s), \quad (15)$$

$$\sigma_{12}(\tilde{\mathbf{u}}_s) = 2 p_{66} e_{12}(\tilde{\mathbf{u}}_s). \quad (16)$$

In a VTI medium $p_{12} = p_{11} - 2p_{66}$, so that only five independent stiffness, that is, $p_{11}, p_{33}, p_{13}, p_{55}$ and p_{66} need to be considered.

Santos & Carcione (2015) have shown that the stiffnesses p_{IJ} in eqs (11)–(16) can be determined using five time-harmonic experiments. Next, we present the generalization of those experiments using the 2PBM to determine a VTI medium long-wave equivalent to a fine layered poroelastic solid saturated by a two-phase fluid.

Denoting by x_1 and x_3 the horizontal and vertical coordinates, we will solve eqs (6)–(8) in the 2-D case on a reference square $\Omega = (0, L)^2$ with boundary Γ in the (x_1, x_3) -plane. Set $\Gamma = \Gamma^L \cup \Gamma^R \cup \Gamma^B \cup \Gamma^T$, where $\Gamma^L, \Gamma^R, \Gamma^B$ and Γ^T denote the left, right, bottom and top boundaries of Ω , respectively. Denote by \mathbf{v} the unit outer normal on Γ and let $\boldsymbol{\chi}$ be a unit tangent on Γ oriented counterclockwise so that $\{\mathbf{v}, \boldsymbol{\chi}\}$ is an orthonormal system on Γ . To determine the five independent stiffness coefficients, we solve eqs (6)–(8) in Ω with the boundary conditions:

$$\mathbf{u}^n \cdot \mathbf{v} = 0, \quad \mathbf{u}^w \cdot \mathbf{v} = (x_1, x_3) \in \Gamma, \quad (17)$$

that is, no fluids enter or leave the sample, and additional boundary conditions for each p_{IJ} .

To determine p_{33} , we impose the boundary conditions:

$$\boldsymbol{\tau}(\mathbf{u})\mathbf{v} \cdot \mathbf{v} = -\Delta P, \quad (x_1, x_3) \in \Gamma^T, \quad (18)$$

$$\boldsymbol{\tau}(\mathbf{u})\mathbf{v} \cdot \boldsymbol{\chi} = 0, \quad (x_1, x_3) \in \Gamma, \quad (19)$$

$$\mathbf{u}^s \cdot \mathbf{v} = 0, \quad (x_1, x_3) \in \Gamma \setminus \Gamma^T. \quad (20)$$

Using the relation

$$\frac{\Delta V(\omega)}{V} = -\frac{\Delta P}{p_{33}(\omega)}, \quad (21)$$

where V is the original volume of the sample, $p_{33}(\omega)$ can be determined from eq. (21) measuring the complex volume change $\Delta V(\omega) \approx Lu_{s,3}^{(33,T)}(\omega)$, where $u_{s,3}^{(33,T)}(\omega)$ is the average of the vertical component of the solid phase at the boundary Γ^T .

To determine p_{11} , the following boundary conditions are used:

$$\boldsymbol{\tau}(\mathbf{u})\mathbf{v} \cdot \mathbf{v} = -\Delta P, \quad (x_1, x_3) \in \Gamma^R, \quad (22)$$

$$\boldsymbol{\tau}(\mathbf{u})\mathbf{v} \cdot \boldsymbol{\chi} = 0, \quad (x_1, x_3) \in \Gamma, \quad (23)$$

$$\mathbf{u}^s \cdot \mathbf{v} = 0, \quad (x_1, x_3) \in \Gamma \setminus \Gamma^R. \quad (24)$$

Thus, this experiment determines p_{11} as indicated for p_{33} , measuring the oscillatory volume change.

To determine p_{13} , we apply the boundary conditions:

$$\boldsymbol{\tau}(\mathbf{u})\mathbf{v} \cdot \mathbf{v} = -\Delta P, \quad (x_1, x_3) \in \Gamma^R \cup \Gamma^T, \quad (25)$$

$$\boldsymbol{\tau}(\mathbf{u})\mathbf{v} \cdot \boldsymbol{\chi} = 0, \quad (x_1, x_3) \in \Gamma, \quad (26)$$

$$\mathbf{u}^s \cdot \mathbf{v} = 0, \quad (x_1, x_3) \in \Gamma^L \cup \Gamma^B. \quad (27)$$

From eqs (11) and (13), we get

$$\sigma_{11} = p_{11}\epsilon_{11} + p_{13}\epsilon_{33} \quad \sigma_{33} = p_{13}\epsilon_{11} + p_{33}\epsilon_{33},$$

with ϵ_{11} and ϵ_{33} being the (macroscale) strain components at Γ^L and Γ^T , respectively. Since $\sigma_{11} = \sigma_{33} = -\Delta P$ (cf. eq. 25) we obtain $p_{13}(\omega)$ as

$$p_{13}(\omega) = \frac{p_{11}\epsilon_{11} - p_{33}\epsilon_{33}}{\epsilon_{11} - \epsilon_{33}}. \quad (28)$$

The stiffness p_{55} is determined by imposing the boundary conditions:

$$-\boldsymbol{\tau}(\mathbf{u})\mathbf{v} = \mathbf{g}, \quad (x_1, x_3) \in \Gamma^T \cup \Gamma^L \cup \Gamma^R, \quad (29)$$

$$\mathbf{u}_s = 0, \quad (x_1, x_3) \in \Gamma^B, \quad (30)$$

where

$$\mathbf{g} = \begin{cases} (0, \Delta G), & (x_1, x_3) \in \Gamma^L, \\ 0, -\Delta G), & (x_1, x_3) \in \Gamma^R, \\ -\Delta G, 0), & (x_1, x_3) \in \Gamma^T. \end{cases}$$

The change in shape of the rock sample allows to obtain $p_{55}(\omega)$ using the relation

$$\text{tg}(\beta\omega) = \frac{\Delta G}{p_{55}(\omega)}, \quad (31)$$

Table 1. Material properties.

Property	Illite/smectite	Kerogen	Water	Oil	Gas
K_s (GPa)	28.4	7	2.25	0.57	0.022
K_m (GPa)	18	4.3	–	–	–
μ_m (GPa)	12.5	1.3	–	–	–
ρ_s (g cm ⁻³)	2.7	1.4	1	0.7	0.078
ϕ (per cent)	10	10	–	–	–
η (cP)	–	–	1	10	0.015
κ (ndarcy)	200	200	–	–	–
S_w (per cent)	99	0	–	–	–
S_o (per cent)	0	90	–	–	–
S_g (per cent)	1	10	–	–	–

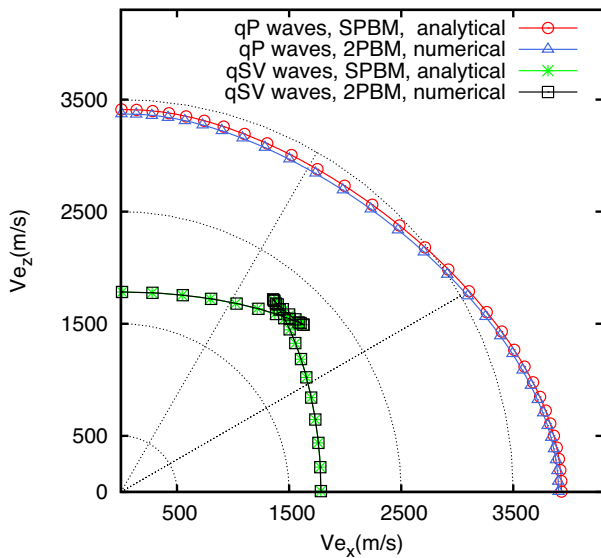


Figure 2. Polar representation of the energy velocities of the qP and qSV waves for the FE 2PBM and analytical SPBM models at 50 Hz. The medium consists of a sequence of nine water–gas saturated illite–smectite layers and one oil–gas saturated kerogen layer (relation 9–1). The results of the analytical model are obtained as effective single-phase fluids.

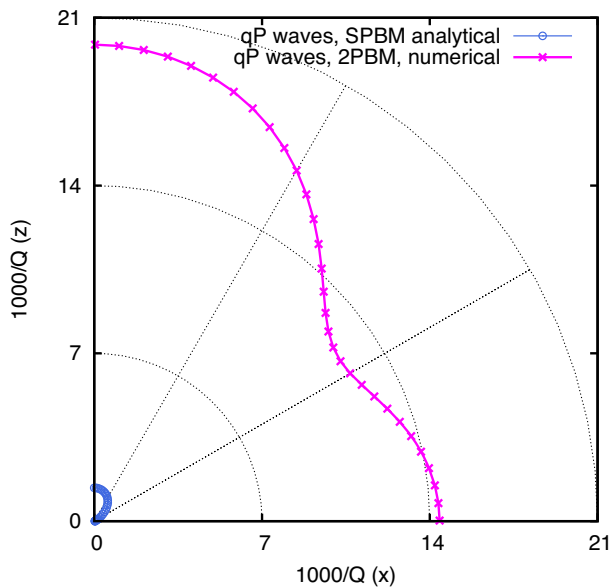


Figure 3. Polar representation of the dissipation factors of the qP waves for the FE 2PBM and analytical SPBM models at 50 Hz. The medium consists of a sequence of nine water–gas saturated illite–smectite layers and one oil–gas saturated kerogen layer. The results of the analytical model are obtained as effective single-phase fluids.

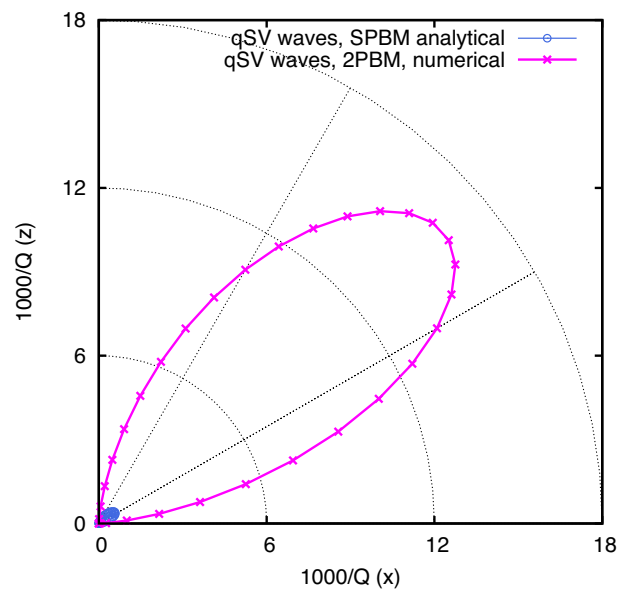


Figure 4. Polar representation of the dissipation factors of the qSV waves for the FE 2PBM and analytical SPBM models at 50 Hz. The medium consists of a sequence of nine water–gas saturated illite–smectite layers and one oil–gas saturated kerogen layer. The results of the analytical model are obtained as effective single-phase fluids.

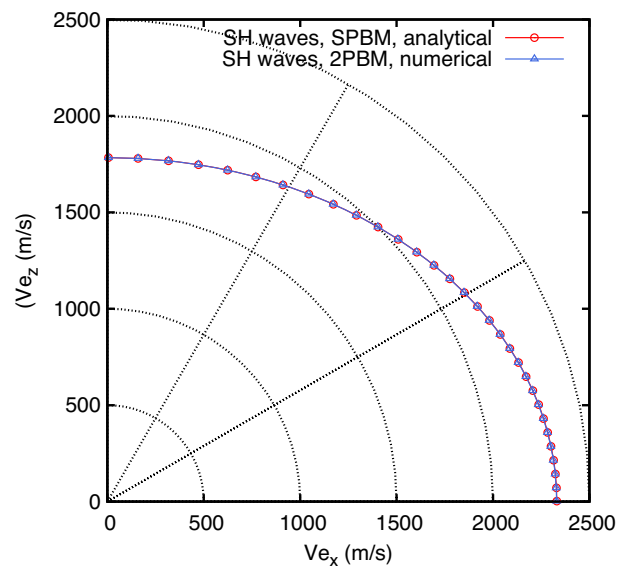


Figure 5. Polar representation of the energy velocities of the SH waves for the FE 2PBM and analytical SPBM models at 50 Hz. The medium consists of a sequence of nine water–gas saturated illite–smectite layers and one oil–gas saturated kerogen layer. The results of the analytical model are obtained as effective single-phase fluids.

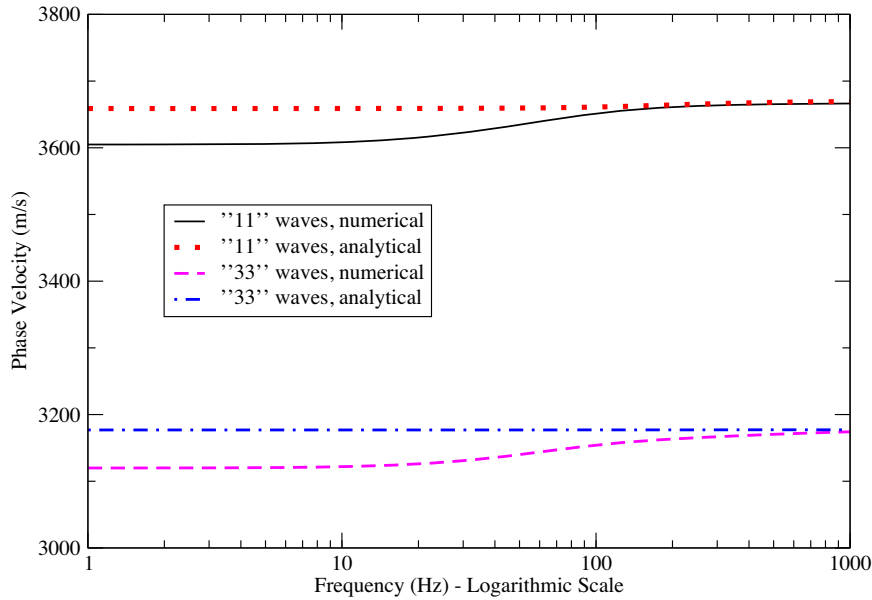


Figure 6. Velocity of waves parallel ('11' waves) and normal ('33' waves) to the layering plane as a function of frequency. The medium consists of a sequence of nine water–gas saturated illite–smectite layers and one oil–gas saturated kerogen layer.

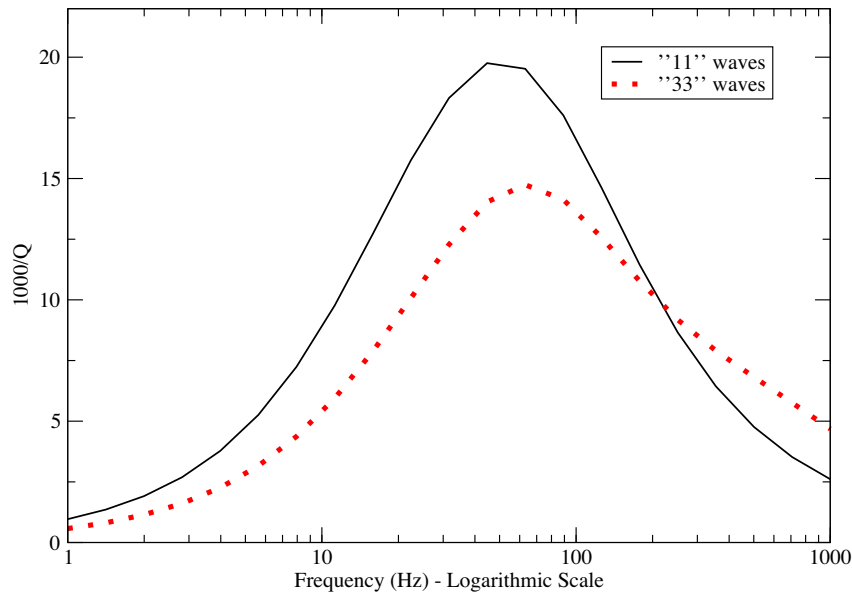


Figure 7. Dissipation factor of waves parallel ('11' waves) and normal ('33' waves) to the layering plane as a function of frequency. The medium consists of a sequence of nine water–gas saturated illite–smectite layers and one oil–gas saturated kerogen layer.

where $\beta(\omega)$ is the departure angle between the original positions of the lateral boundaries and those after applying the shear stresses, which can be determined by measuring the average horizontal displacement at Γ^T (Santos & Carcione 2015).

Finally, the stiffness p_{66} is obtained using the boundary conditions:

$$-\boldsymbol{\tau}(\mathbf{u})\boldsymbol{\nu} = \mathbf{g}_2, \quad (x_1, x_2) \in \Gamma^B \cup \Gamma^R \cup \Gamma^T, \quad (32)$$

$$\mathbf{u}_s = 0, \quad (x_1, x_2) \in \Gamma^L, \quad (33)$$

where

$$\mathbf{g}_2 = \begin{cases} (\Delta G, 0), & (x_1, x_2) \in \Gamma^B, \\ -\Delta G, 0), & (x_1, x_2) \in \Gamma^T, \\ 0, -\Delta G), & (x_1, x_2) \in \Gamma^R. \end{cases}$$

Then, we proceed as indicated for $p_{55}(\omega)$.

The approximate solution of these five BVP was computed using an FE procedure. On each cell of the FE partition of the computational domain, we used bilinear functions to approximate each component of the solid displacement vector, while for the non-wetting and wetting fluid displacements we used a closed subspace of the vector part of the Raviart–Thomas–Nedelec space of zero order (Raviart & Thomas 1975). See Santos & Carcione (2015) and Santos & Gauzellino (2017) for details on the description of

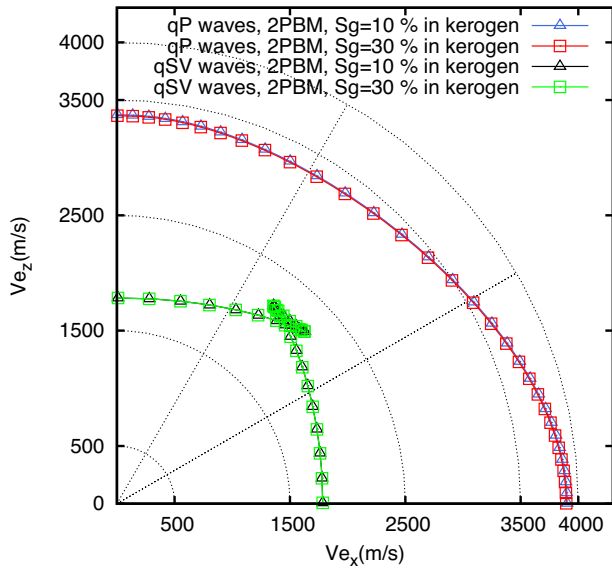


Figure 8. Polar representation of the energy velocities of the qP and qSV waves for the FE 2PBM model at 50 Hz as a function of gas saturation in kerogen layers. The medium consists of a sequence of nine water–gas saturated illite–smectite layers and one oil–gas saturated kerogen layer.

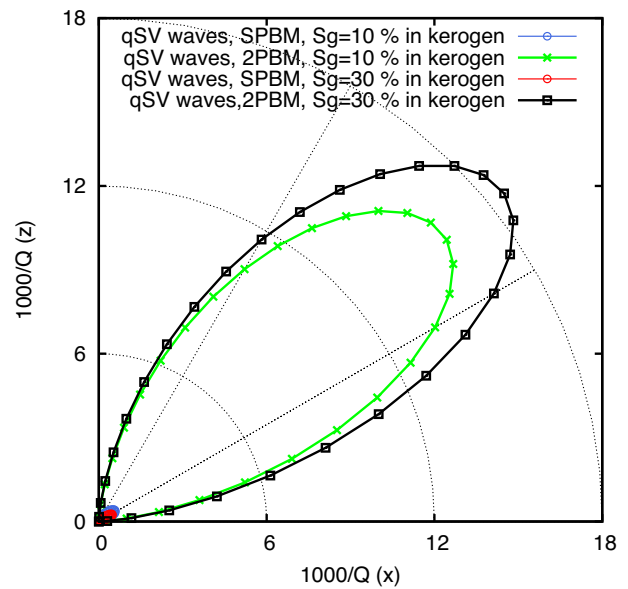


Figure 10. Polar representation of dissipation factors of the qSV waves for the FE 2PBM model at 50 Hz as a function of gas saturation in kerogen layers. The medium consists of a sequence of nine water–gas saturated illite–smectite layers and one oil–gas saturated kerogen layer.

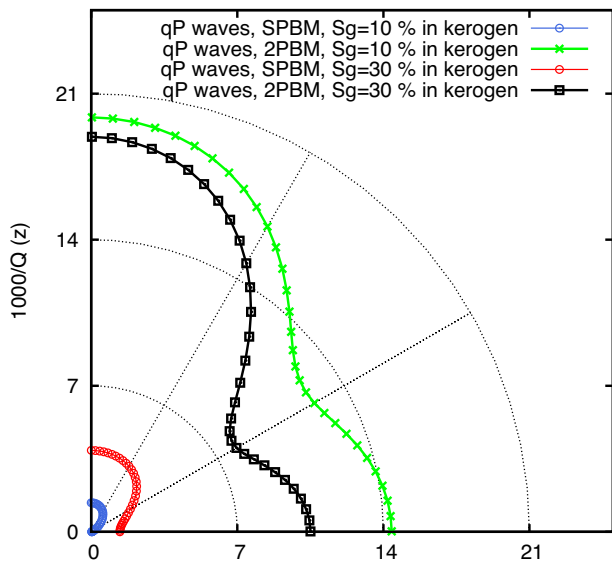


Figure 9. Polar representation of the dissipation factors of the qP waves for the FE 2PBM model at 50 Hz as a function of gas saturation in kerogen layers. The medium consists of a sequence of nine water–gas saturated illite–smectite layers and one oil–gas saturated kerogen layer.

these FE spaces. Also, it was shown in Santos & Carcione (2015) that the error associated with these FE problems, measured in the energy norm, is on the order of $h^{1/2}$, with h being the size of the computational mesh. The proof can be generalized to the case of two-phase fluids analysed here.

4 NUMERICAL METHODOLOGY

The five complex stiffnesses $p_{IJ}(\omega)$, as a function of the frequency and propagation direction, are determined by solving the associated BVP using the FE method. The corresponding energy velocities

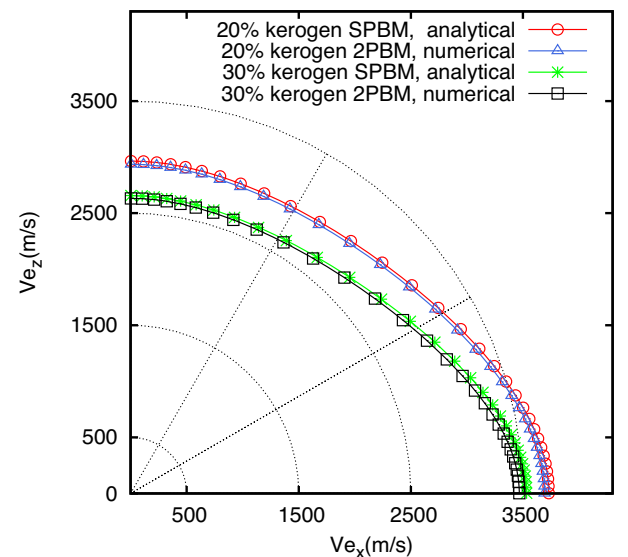


Figure 11. Polar representation of the energy velocities of the qP waves for the FE 2PBM and SPBM models at 50 Hz as a function of kerogen concentration. The medium consists of a sequence of eight (seven) water–gas saturated illite–smectite layers and two (three) oil–gas saturated kerogen layer. $S_g = 10$ per cent in the illite–smectite and kerogen layers.

and dissipation factors for qP , qSV and SH waves are obtained as in appendices A and B of Santos & Carcione (2015).

The FE experiments consider square periodic layered samples Ω of side length 0.09 cm with six periods of illite–smectite and kerogen layers (see Fig. 1), discretized using a 60×60 uniform mesh, that is, $\Omega = \cup_j \Omega_j$. The material properties are given in Table 1.

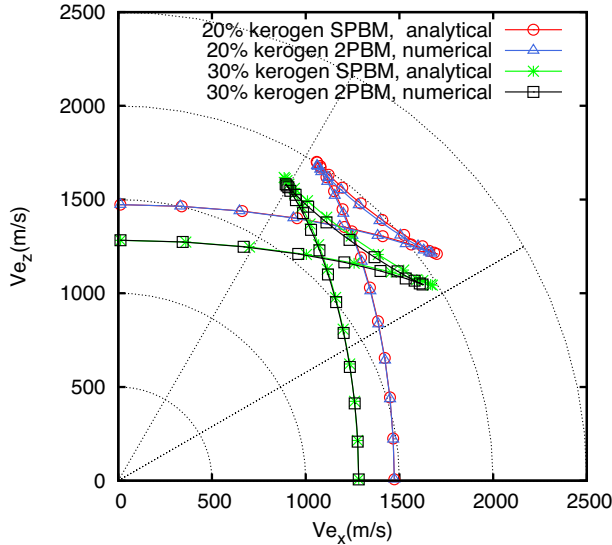


Figure 12. Polar representation of the energy velocities of the qSV waves for the FE 2PBM and SPBM models at 50 Hz as a function of kerogen concentration. The medium consists of a sequence of eight (seven) water–gas saturated illite–smectite layers and two (three) oil–gas saturated kerogen layer. $S_g = 10$ per cent in the illite–smectite and kerogen layers.

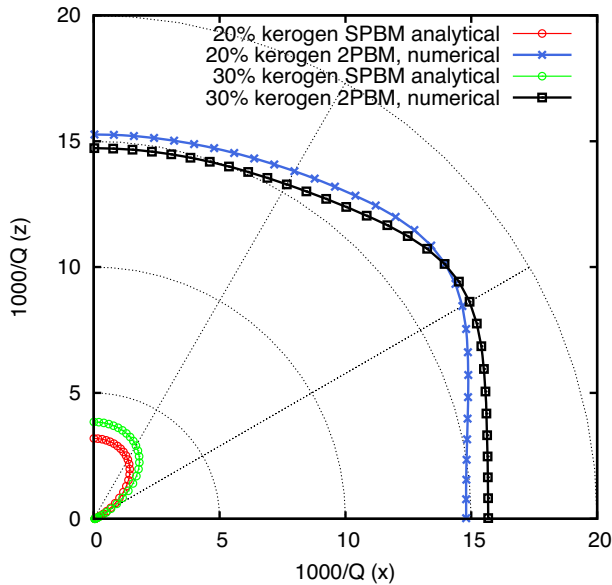


Figure 13. Polar representation of the dissipation factors of the qP waves for the FE 2PBM and SPBM models at 50 Hz as a function of kerogen concentration. The medium consists of a sequence of eight (seven) water–gas saturated illite–smectite layers and two (three) oil–gas saturated kerogen layer. $S_g = 10$ per cent in the illite–smectite and kerogen layers.

4.1 Numerical simulations

The experiments consider a square sample of side length 0.09 cm with an alternating sequence of 0.0135 cm of illite–smectite and 0.0015 cm of kerogen layers, each layer saturated by a two-phase fluid. In the illite–smectite layers, the wetting and non-wetting phases are water and gas, with residual saturations $S_{rw} = 4.5$ per cent and $S_{rg} = 0$, respectively, and gas saturation is $S_g = 1$ per cent. In the kerogen layers, the wetting and non-wetting phases are oil and gas, with residual saturations $S_{rw} = S_{ro} = 4.5$ per cent

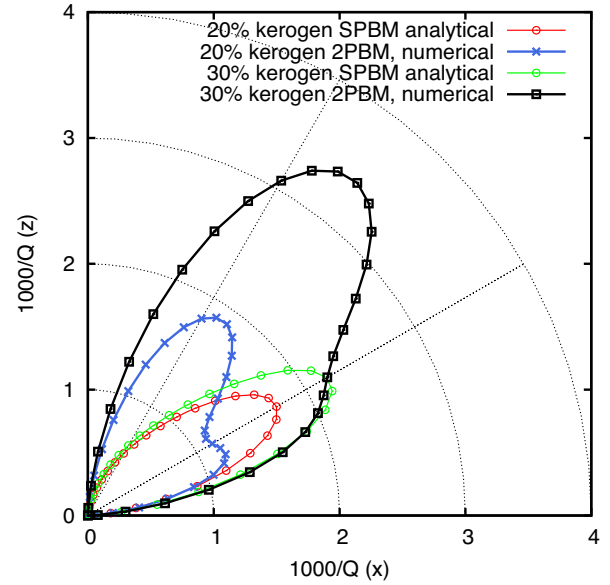


Figure 14. Polar representation of the dissipation factors of the qSV waves for the FE 2PBM and SPBM models at 50 Hz as a function of kerogen concentration. The medium consists of a sequence of eight (seven) water–gas saturated illite–smectite layers and two (three) oil–gas saturated kerogen layer. $S_g = 10$ per cent in the illite–smectite and kerogen layers.

and $S_{rg} = 0$, respectively, and gas saturation is $S_g = 10$ per cent. Thus, in these experiments $S_m = S_{rg}$.

The experiments compare energy velocities (Santos *et al.* 2014) and dissipation factors of qP , qSV and SH waves computed using the 2PBM, when the sample is saturated by a two-phase fluid mixture, with the velocities obtained with the analytical solution using the SPBM model as in Krzikalla & Müller (2011). The properties of the single-phase fluids are determined by weighting those of the water–gas and the oil–gas mixtures with the corresponding saturations. The effective single-phase fluid viscosity $\eta^{(eff)}$ and density $\rho^{(eff)}$ are obtained as arithmetic averages of those of the water–gas or oil–gas viscosities, while the effective bulk modulus $K^{(eff)}$ was determined using a Reuss average of the water–gas or oil–gas bulk moduli:

$$\begin{aligned} \eta^{(eff)} &= \eta_n S_n + \eta_w S_w, \\ \rho^{(eff)} &= \rho_n S_n + \rho_w S_w, \\ \frac{1}{K^{(eff)}} &= \frac{S_n}{K_n} + \frac{S_w}{K_w}. \end{aligned}$$

Small differences between energy velocities of the qP and qSV waves at 50 Hz for the FE 2PBM and analytical models can be observed due to capillary pressure and relative permeability effects present in the 2PBM (Fig. 2). The dissipation factors of the qP and qSV waves are much higher for the 2PBM than for the SPBM (Figs 3 and 4). Furthermore, attenuation is higher at angles between 60 and 90 deg for qP waves and at angles between 30 and 60 deg for qSV waves.

The higher attenuation predicted by the 2PBM model is due to the combined effects of relative permeability and capillary pressure. Relative permeabilities define the dissipation function in the Lagrangian formulation of the 2PBM (Santos *et al.* 1990a), and they represent the interaction between the two fluid phases as they move within the pore space. To quantify this effect, we have computed the L^2 norm of the horizontal and vertical displacements of both fluid phases for the p_{11} and p_{33} tests. For the p_{11} test, the L^2 norm of the horizontal displacement of the non-wetting phase is higher than that

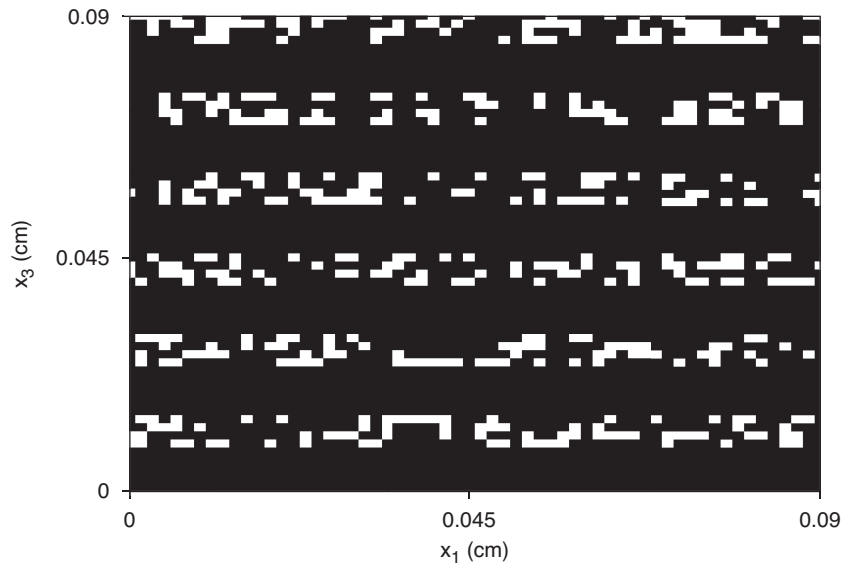


Figure 15. Patchy gas saturation distribution in the kerogen layers. The white regions correspond to $S_g = 30$ percent, the black regions correspond to $S_g = 1$ percent. Overall gas saturation in the kerogen layers is 10 percent. The sample is a square of side length 0.09 cm.

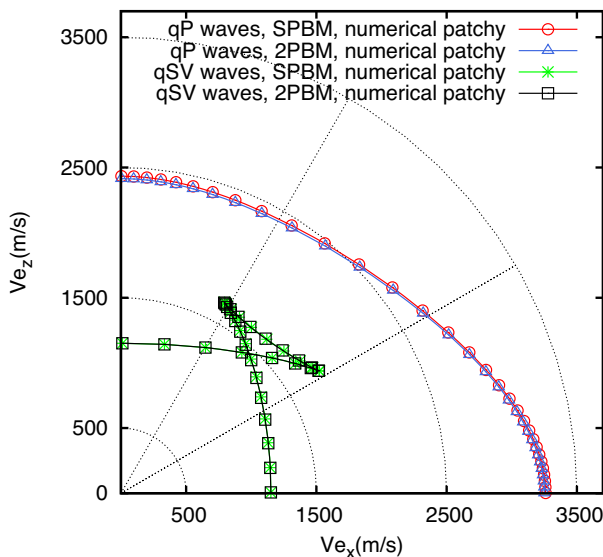


Figure 16. Polar representation of energy velocities of the qP and qSV waves for the FE 2PBM and FE SPBM models at 50 Hz. Patchy gas-oil distribution in the kerogen layers with overall gas saturation $S_g = 10$ percent. The medium consists of a sequence of six water-gas saturated illite-smectite layers and four oil-gas saturated kerogen layer (Kerogen concentration is 40 percent). $S_g = 1$ percent in the illite-smectite layers.

of the wetting phase, while for the p_{33} experiment this behaviour was observed for the vertical displacements. The same behaviour of the displacements of the two fluid phases was observed in all the experiments performed in this section. These relative motions between the two fluid phases induce energy losses not present in single-phase fluids.

The energy velocities of SH waves are not affected by the relative permeability and capillary pressure (Fig. 5). This behaviour is explained by the fact that SH waves are uncoupled of the qP waves and the shear experiment associated with the SH waves does not induce changes in fluid pressure.

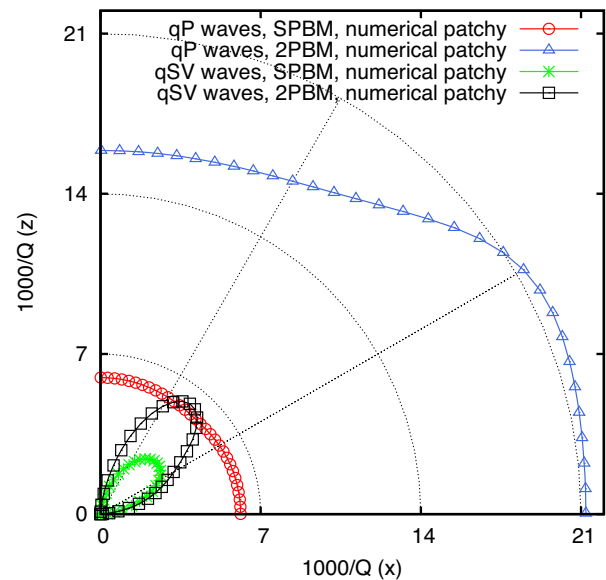


Figure 17. Polar representation of dissipation factors of the qP and qSV waves for the FE 2PBM and FE SPBM models at 50 Hz. Patchy gas-oil distribution in the kerogen layers with overall gas saturation $S_g = 10$ percent with . The medium consists of a sequence of six water-gas saturated illite-smectite layers and four oil-gas saturated kerogen layer (Kerogen concentration is 40 percent). $S_g = 1$ percent in the illite-smectite layers.

Next, we analyse the behaviour of the phase velocities and dissipation factors of waves as they travel parallel and normal to the layers as function of frequency. In particular, this study allows to identify the possible existence and location of attenuation peaks. The following experiment analyses the behaviour of waves as a function of frequency in the range 1 Hz–1 kHz. Fig. 6 displays velocities of waves parallel ('11' waves) and normal ('33' waves) to the layering plane, while Fig. 7 shows the corresponding dissipation factors. Velocities increase with frequency. Furthermore, '11' waves exhibit higher phase velocities than '33' waves. Dissipation

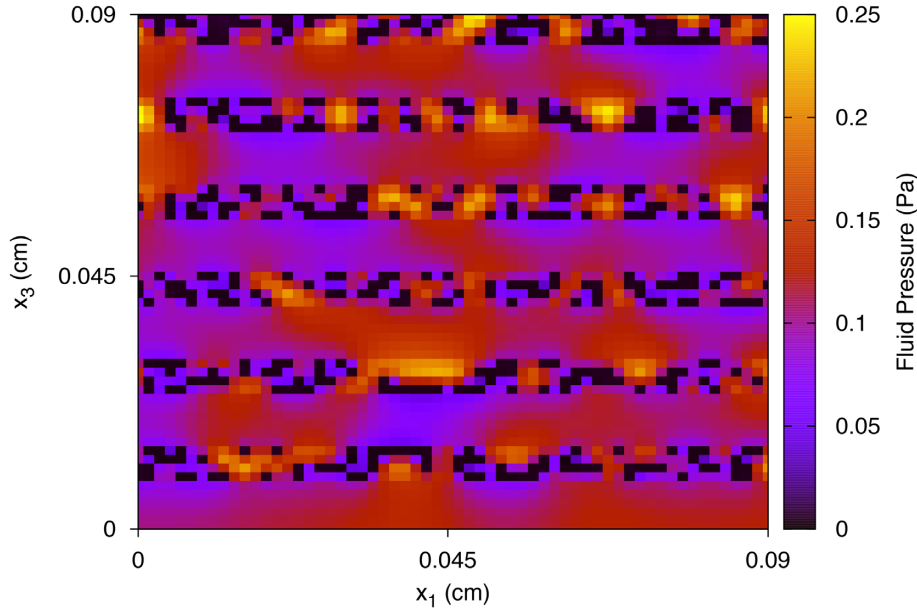


Figure 18. Absolute value of the fluid pressure for the 2PBM model at 50 Hz, patchy gas–oil saturation with 10 per cent overall patchy gas saturation in the kerogen layers. The medium consists of a sequence of six water–gas saturated illite–smectite layers and four oil–gas saturated kerogen layer (Kerogen concentration is 40 per cent). $S_g = 1$ per cent in the illite–smectite layers.

factors are frequency dependent with attenuation peaks of associated quality factors $Q = 50$ at about 50 Hz for ‘11’ waves and $Q = 67$ at about 60 Hz for ‘33’ waves.

In reservoir rocks saturated by two-phase water–gas or oil–gas mixtures, a certain percentage of immobile water or oil (the wetting phases) always exists, indicated by the residual wetting saturation S_{rw} . Thus, in the analysis that follows, the residual saturations are $S_{rg} = 0$, $S_{rw} = 10$ per cent.

4.2 Sensitivity to gas saturation in kerogen layers

To analyse changes in energy velocities and dissipation factors due to variations of gas saturation in the kerogen layers, we consider the same sample of the validation experiments but $S_g = 10$ and 30 per cent in the kerogen layers. The energy velocities of the qP and qSV waves for the 2PBM are not sensitive to changes in gas saturation in the kerogen layers (Fig. 8). The corresponding values of the energy velocities for the SPBM are not shown due to their small differences with those of the 2PBM.

The dissipation factors of the qP and qSV waves as a function of the propagation angle at 50 Hz are shown in Figs 9 and 10, respectively. For qP waves, attenuation is higher for waves travelling normal to the layering plane, and higher for $S_g = 10$ per cent than for $S_g = 30$ per cent. The attenuation predicted by the SPBM model exhibits a similar behaviour but with much lower values.

For qSV waves, attenuation is stronger for angles between 30 and 60 deg, and higher for $S_g = 30$ per cent than for $S_g = 10$ per cent. Attenuation values obtained using the SPBM model are negligible and are shown as a point at the origin. As in the previous example, relative permeabilities are responsible for the high attenuation predicted by the 2PBM model.

4.3 Sensitivity to kerogen concentration

Here, we analyse changes in the energy velocities and dissipation factors of qP and qSV waves due to variations in the kerogen

concentration. We consider the same sample of the validation experiments with six periods of 0.012 cm of illite–smectite and 0.003 cm of kerogen (20 per cent kerogen) and six periods of 0.0105 cm of illite–smectite and 0.0045 cm of kerogen (30 per cent kerogen). As expected, lower velocity corresponds to higher kerogen content (Figs 11 and 12). Furthermore, much higher dissipation factors are observed for the 2PBM model than for the SPBM model, and a completely different anisotropic behaviour (Figs 13 and 14). These results indicate that the SPBM model is not reliable for predicting attenuation in multiphase saturated porous rocks.

4.4 Sensitivity to patchy saturation

Finally, we analyse the effect of patchy gas–oil saturation in the kerogen layers for the case of 40 per cent kerogen concentration. Patchy-saturation patterns produce strong mesoscopic-loss effects at the seismic frequency band, as shown by White *et al.* (1975).

To generate patchy gas–oil distribution in the kerogen layers, we proceed as follows. The first step to generate a patchy fluid distribution is to assign to each subdomain Ω_j , of the partition of the domain Ω , a pseudo-random number using a generator with uniform distribution. This random field is Fourier transformed to the spatial wavenumber domain and its amplitude spectrum is multiplied by the von Karman spectral density given by (Frankel & Clayton 1986; Santos *et al.* 2005)

$$S_d(k_{x_1}, k_{x_3}) = S_0(1 + k^2(CL)^2)^{-(H+N_e/2)}, \tag{34}$$

where $k = \sqrt{(k_{x_1})^2 + (k_{x_3})^2}$ is the radial wavenumber, N_e is the Euclidean dimension, CL the correlation length, H is a self-similarity coefficient ($0 < H < 1$) and S_0 is a normalization constant. Eq. (34) corresponds to a fractal process of dimension $D = N_e + 1 - H$ at scales smaller than CL . The resulting fractal spectrum is then transformed back to the spatial domain, obtaining a *microheterogeneous* fractal gas saturation model $S_g^{(j)}$.

Next, to assign to each cell Ω^j either $S_g = 1$ per cent or $S_g = 30$ per cent, a threshold value S_g^* is chosen so that for each subdomain Ω_j where $S_g^{(j)} \leq S_g^*$ it is assumed that such subdomain has $S_g = 1$ per cent, while if $S_g^{(j)} > S_g^*$, $S_g = 30$ per cent in Ω_j . In this way, a multiscale binary gas–oil patchy-saturation model is constructed and an overall brine saturation \bar{S}_g is obtained. In the examples, the fractal dimension is $D = 2.3$ and the correlation length is 1.67 per cent of the side length of the sample. Residual saturations are $S_{rw} = 10$ per cent and $S_{rg} = 0$. Saturation in the illite–smectite layers is chosen to be uniform with gas saturation $S_g = 1$ per cent.

Fig. 15 displays the patchy gas–oil distribution in the kerogen layers. The white regions correspond to $S_g = 30$ per cent, and the black regions correspond to $S_g = 1$ per cent. Figs 16 and 17 show the energy velocities and dissipation factors of qP and qSV waves at 50 Hz for the SPBM and 2PBM models and patchy gas–oil saturation in the kerogen layers for overall gas saturation 10 per cent. The results of the SPBM were obtained using the FE harmonic experiments as in Picotti *et al.* (2010) with the effective single-phase fluid properties determined as in eq. (34).

Energy velocities of qP and qSV waves are very similar for both models (Fig. 16). On the other hand, the attenuation of the qP waves is almost isotropic for the SPBM model, while the 2PBM model exhibits much higher attenuation and strong anisotropy (Fig. 17). Furthermore, qSV attenuation is strong for angles between 30 and 60 deg and higher for the 2PBM model than for the SPBM model.

Fig. 18 shows the absolute value of the total fluid pressure distribution \tilde{T} at 50 Hz, defined as $\tilde{T} = \mathcal{T}_n + \mathcal{T}_w$, with \mathcal{T}_n and \mathcal{T}_w being the generalized forces in eqs (3) and (4), respectively. It is seen that pressure gradients are the highest at the gas–oil interfaces. This illustrates the WIFF mechanism.

5 CONCLUSIONS

We have shown that in porous rocks saturated with two-phase fluids, the presence of capillary forces (interfacial tension) and the relative permeabilities, significantly affect the attenuation of qP and qSV waves. We considered shales composed of illite–smectite layers saturated with water and gas, and kerogen layers saturated with oil and gas. Quasi-static numerical experiments performed with an FE procedure allowed us to compute the energy velocities and dissipation factors due to WIFF. The higher attenuation and strong Q anisotropy predicted by the 2PBM are due to the combined effects of relative permeability and capillary pressure. Relative permeabilities define the dissipation function in the Lagrangian formulation, representing the interaction between the two fluid phases as they move within the pore space. These relative motions induce energy losses not present in rock saturated with single-phase or effective fluids.

REFERENCES

- Auriault, J.L., Lebaigue, O. & Bonnet, G., 1989. Dynamics of two immiscible fluids flowing through deformable porous media, *Transp. Porous Media*, **4**, 105–128.
- Berryman, J., Thigpen, L. & Chin, R., 1988. Bulk elastic wave propagation in partially saturated porous solids, *J. acoust. Soc. Am.*, **84**, 360–373.
- Biot, M.A., 1956a. Theory of propagation of elastic waves in a fluid-saturated porous solid. I. Low frequency range, *J. acoust. Soc. Am.*, **28**, 168–178.
- Biot, M.A., 1956b. Theory of propagation of elastic waves in a fluid-saturated porous solid. II. High frequency range, *J. acoust. Soc. Am.*, **28**, 179–191.
- Biot, M.A., 1962. Mechanics of deformation and acoustic propagation in porous media, *J. Appl. Phys.*, **33**, 1482–1498.
- Bouzidi, Y. & Schmitt, D., 2009. Measurement of the speed and attenuation of the Biot slow wave using a large ultrasonic transmitter, *J. geophys. Res.*, **114**, B08201, doi:10.1029/2008JB006018
- Carcione, J.M., 2014. *Wave Fields in Real Media. Theory and Numerical Simulation of Wave Propagation in Anisotropic, Anelastic, Porous and Electromagnetic Media*, 3rd edn, Elsevier, revised and extended.
- Carcione, J.M. & Picotti, S., 2006. P-wave seismic attenuation by slow-wave diffusion: effects of inhomogeneous rock properties, *Geophysics*, **71**, O1–O8.
- Carcione, J.M., Kosloff, D. & Behle, A., 1991. Long wave anisotropy in stratified media: a numerical test, *Geophysics*, **56**, 245–254.
- Carcione, J.M., Helle, H.B. & Avseth, P., 2011. Source-rock seismic-velocity models: Gassmann versus Backus, *Geophysics*, **76**, N37–N45.
- Dutta, N.C. & Odé, H., 1979. Attenuation and dispersion of compressional waves in fluid-filled porous rocks with partial gas saturation (White model)—Part I: Biot theory, *Geophysics*, **44**, 1777–1788.
- Frankel, A. & Clayton, R.W., 1986. Finite difference simulation of seismic wave scattering: implications for the propagation of short period seismic waves in the crust and models of crustal heterogeneity, *J. geophys. Res.*, **91**, 6465–6489.
- Gelinsky, S. & Shapiro, S.A., 1997. Poroelastic Backus-averaging for anisotropic, layered fluid and gas saturated sediments, *Geophysics*, **62**, 1867–1878.
- Krzikalla, F. & Müller, T.M., 2011. Anisotropic P-SV-wave dispersion and attenuation due to interlayer flow in thinly layered porous rocks, *Geophysics*, **76**, WA135, doi:10.1190/1.3555077.
- Mochizuki, S., 1982. Attenuation in partially saturated rocks, *J. geophys. Res.*, **87**, 8598–8604.
- Müller, T.M. & Sahay, P., 2011. Fast compressional wave attenuation and dispersion due to conversion scattering into slow shear waves in randomly heterogeneous porous media, *J. acoust. Soc. Am.*, **129**(5), 2785–2796.
- Müller, T.M., Gurevich, G. & Lebedev, M., 2010. Seismic wave attenuation and dispersion resulting from wave-induced flow in porous rocks—a review, *Geophysics*, **75**(5), 75A147–75A164.
- Peaceman, D.W., 1977. *Fundamentals of Numerical Reservoir Simulation*, Elsevier.
- Picotti, S., Carcione, J.M., Santos, J.E. & Gei, D., 2010. Q-anisotropy in finely-layered media, *Geophys. Res. Lett.*, **37**(6), L06302, doi:10.1029/2009GL042046.
- Plona, T.J., 1980. Observation of a second bulk compressional wave in a porous medium at ultrasonic frequencies, *Appl. Phys. Lett.*, **56**, 259–261.
- Pride, S., Berryman, J. & Harris, J., 2004. Seismic attenuation due to wave-induced flow, *J. geophys. Res.*, **109**, B01201, doi:10.1029/2003JB002639.
- Qi, Q., Müller, T., Gurevich, M.B., Lopes, S., Lebedev, M. & Caspari, E., 2014. Quantifying the effect of capillarity on attenuation and dispersion in patchy-saturated rocks, *Geophysics*, **79**, WB35–WB50.
- Ravazzoli, C.L., Santos, J.E. & Carcione, J.M., 2003. Acoustic and mechanical response of reservoir rocks under variable saturation and effective pressure, *J. acoust. Soc. Am.*, **113**, 1801–1811.
- Raviart, P.A. & Thomas, J.M., 1975. Mixed finite element method for second order elliptic problems, in *Mathematical Aspects of the Finite Element Methods*, Lecture Notes of Mathematics, eds Galligani, I. & Magenes, E., Springer, 292–315.
- Santos, J.E. & Carcione, J.M., 2015. Finite-element harmonic experiments to model fractured induced anisotropy in poroelastic media, *Comput. Methods Appl. Mech. Eng.*, **283**, 1189–1213.
- Santos, J.E. & Gauzellino, P.M., 2017. *Numerical Simulation in Applied Geophysics*, Birkhauser, Lecture Notes in Geosystems Mathematics and Computing, Springer.
- Santos, J.E., Corberó, J.M. & Douglas, J., Jr, 1990a. Static and dynamic behaviour of a porous solid saturated by a two-phase fluid, *J. acoust. Soc. Am.*, **87**, 1428–1438.
- Santos, J.E., Douglas, J., Jr, Corberó, J. & Lovera, O.M., 1990b. A model for wave propagation in a porous medium saturated by a two-phase fluid, *J. acoust. Soc. Am.*, **87**, 1439–1448.

- Santos, J.E., Ravazzoli, C.L., Gauzellino, P.M. & Carcione, J.M., 2005. Numerical simulation of ultrasonic waves in reservoir rocks with patchy saturation and fractal petrophysical properties, *Comput. Geosci.*, **9**, 1–27.
- Santos, J.E., Martinez Corredor, R. & Carcione, J.M., 2014. Seismic velocity and *Q* anisotropy in fractured poroelastic media, *Int. J. Rock Mech. Min. Sci.*, **70**, 212–218.
- Scheidegger, A.E., 1974. *The Physics of Flow through Porous Media*, University of Toronto.
- Toksöz, M.N., Cheng, C.H. & Timur, A., 1976. Velocities of seismic waves in porous rocks, *Geophysics*, **41**, 621–645.
- White, J.E., Mikhaylova, N.G. & Lyakhovitskiy, F.M., 1975. Low-frequency seismic waves in fluid-saturated layered rocks, *J. acoust. Soc. Am.*, **57**, doi:10.1121/1.1995164.